International Journal of Nanomedicine

Dovepress
Taylor & Francis Group

Open Access Full Text Article

ORIGINAL RESEARCH

# Quantifying Nanoplastic Toxicity Using Gold-Core Polystyrene Nanoparticles: In vivo Evaluation and Human Risk Extrapolation

Yingzi Cui[1,*], Xiaohan Tong[1,*], Jiawang Ding[2], Boqing Li[1], Wenke Wang[1], Chunlei Ma[1], Zhiqin Li[1], Ying Zhang[1]

[1]School of Basic Medical Sciences, Binzhou Medical University, Yantai, Shandong, People's Republic of China; [2]CAS Key Laboratory of Coastal Environmental Processes and Ecological Remediation, Yantai Institute of Coastal Zone Research, Chinese Academy of Sciences, Yantai, Shandong, People's Republic of China

*These authors contributed equally to this work

Correspondence: Ying Zhang; Boqing Li, School of Basic Medicine, Binzhou Medical University, 346 Guanhai Road, Yantai, Shandong, People's Republic of China, Tel +86 535 6913209; +86 535 6913069, Email zhangying@bzmc.edu.cn; liboqing@bzmc.edu.cn



**Purpose:** Nanoplastics (NPs) are widespread environmental pollutants that pose risks to human health; however, risk thresholds for NPs accumulation in human tissues remain poorly defined. This study validates gold-core polystyrene nanoplastics (AuPS-NPs) as a quantifiable proxy for polystyrene nanoplastics (PS-NPs) to evaluate toxicity and bioaccumulation at environmentally relevant concentrations, with extrapolation to human health implications.

**Methods:** AuPS-NPs were synthesized with a gold core and polystyrene shell, characterized by transmission electron microscopy (TEM) and quantified by inductively coupled plasma mass spectrometry (ICP-MS). In vitro, human gastric adenocarcinoma (AGS) and human colorectal adenocarcinoma (Caco-2) cells were exposed to AuPS-NPs or PS-NPs to assess cytotoxicity, reactive oxygen species generation, and mitochondrial membrane depolarization. In vivo, BALB/c mice were orally exposed to AuPS-NPs (1 and 10 mg/L) for 98 days, followed by evaluation of intestinal accumulation, body weight, organ indices, and biomarkers of inflammation, lipid metabolism, energy metabolism, and oxidative stress. A toxicokinetic–toxicodynamic (TK–TD) model was developed to simulate NPs accumulation, dose–response relationships, and human risk thresholds.

**Results:** AuPS-NPs and PS-NPs showed comparable concentration-dependent cytotoxicity in vitro. In vivo, chronic AuPS-NP exposure caused intestinal accumulation, body weight reduction, increased organ indices, and biomarker perturbations including interleukin-6 (IL-6), tumor necrosis factor alpha (TNF-α), triglycerides (TG), total cholesterol (T-CHO), adenosine triphosphate (ATP), lactate dehydrogenase (LDH), malondialdehyde (MDA), and superoxide dismutase (SOD). TK–TD modeling yielded a human intestinal toxicity threshold of $9.529 \times 10^5$ particles/kg, providing a particle-based reference for risk extrapolation.

**Conclusion:** AuPS-NPs replicate PS-NPs toxicity and enable quantitative risk assessment. Chronic exposure may induce intestinal accumulation and systemic toxicity, underscoring the need for regulatory thresholds to mitigate nanoplastic risks.

**Keywords:** polystyrene nanoplastics, toxicokinetics, toxicodynamics, human health risk assessment

## Introduction

Global plastic production has reached alarming levels, amounting to hundreds of millions of tons annually.[1–3] Over time, plastic waste breaks down into smaller fragments, fibers, or debris, collectively referred to as microplastics (MPs, 1 μm–5 mm), through processes such as photo-oxidation, mechanical abrasion, and biodegradation. These MPs can further degrade into NPs (< 1 μm).[4,5] As an emerging class of environmental contaminants, NPs are widely distributed across various matrices, including surface water, sea salt, drinking water, and air.[6–9] Due to their nanoscale size and widespread presence, NPs can cross biological barriers and accumulate in vital organs such as stomach, intestine, and liver.[10–12]

Received: 16 September 2025
Accepted: 23 December 2025
Published: 30 December 2025

**Graphical Abstract**

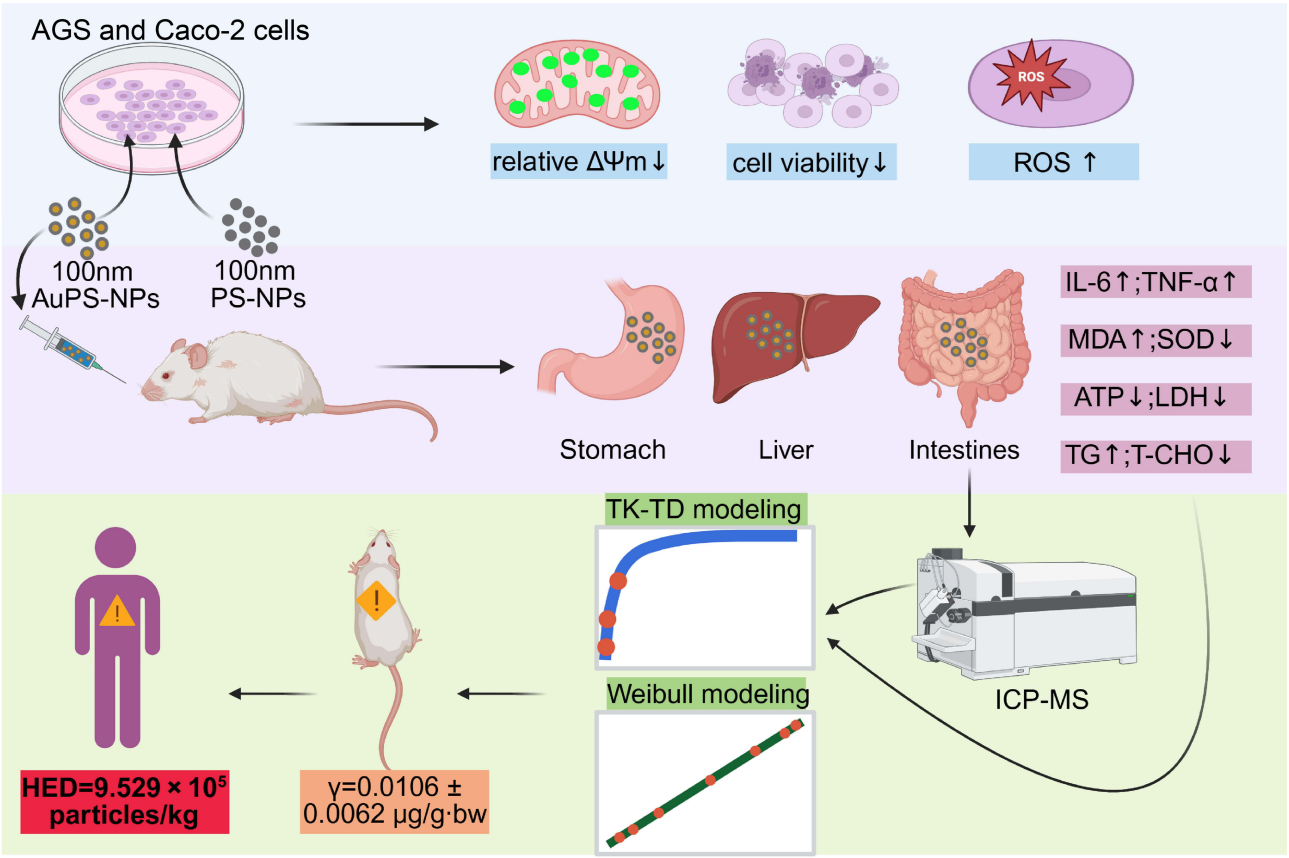


Exposure to NPs has been linked to inflammation, oxidative stress, and metabolic dysfunction in mammalian systems.[13–18] However, current risk assessment efforts remain severely constrained by methodological limitations. The nanoscale size of NPs and their lack of intrinsic markers make accurate quantification in biological matrices challenging.[19,20] In addition, conventional techniques such as fluorescence microscopy lack the sensitivity needed to detect NPs at environmentally relevant concentrations.[19] Furthermore, many studies rely on exposure levels that do not accurately represent real-world human exposure.[13] These challenges collectively impede the establishment of reliable dose-response relationships, which are critical for human health risk assessment.

To address the analytical limitations in quantifying NPs in vivo, we developed AuPS-NPs as an adequate substitute for conventional PS-NPs. AuPS-NPs consist of a gold nanoparticle core encapsulated within a dense polystyrene shell and exhibit physicochemical properties comparable to those of PS-NPs, including long-term stability and similar biodistribution behavior.[21,22] These nanoparticles demonstrate remarkable stability under physiologically harsh conditions while retaining the ability to cross intestinal barriers and enter the systemic circulation.[21] Critically, the embedded gold core enables highly sensitive and organ-specific quantification using inductively coupled plasma mass spectrometry (ICP-MS, detection limit: 0.2 ng/g tissue),[22] rendering AuPS-NPs both biologically representative and analytically traceable for comprehensive biodistribution and toxicity studies.

The toxicokinetic-toxicodynamic (TK-TD) model quantifies NPs behavior within organisms and their dynamic biological effects over time, providing a robust framework for risk assessment.[23] This approach is particularly valuable for studying NPs, as it integrates temporal accumulation patterns with physiological responses while accounting for interspecies differences in nanoparticle processing.[23] By linking external exposure levels to tissue-specific doses and biological outcomes, the model enables extrapolation from controlled experiments to real-world human exposure scenarios. In this study, we aimed to (1) validate

the toxicological equivalence between AuPS-NPs and conventional PS-NPs in vitro using cell viability, oxidative stress, and mitochondrial membrane potential assays; (2) assess in vivo accumulation and toxicity of AuPS-NPs under environmentally relevant exposure concentrations in murine models; and (3) apply a TK-TD model to extrapolate toxicity thresholds to human health risk estimates. We hypothesized that AuPS-NPs faithfully replicate the biological behavior and toxicity profile of PS-NPs while allowing precise quantification, thus offering a robust platform for defining dose–response relationships and informing accurate human health risk assessments for NPs.

# Materials and Methods

## Synthesis and Characterization of PS-NPs and AuPS-NPs

The PS-NPs (diameter: 100 nm) were purchased from Bangs Laboratories (Fishers, IN, USA). AuPS-NPs were synthesized by coating gold nanospheres with polystyrene. Gold seeds were prepared by adding 1.0 mL of sodium citrate (1 wt%) to 100 mL of boiling $HAuCl_4$ (0.01 wt%) under reflux for 30 min. After cooling, 4.0 mL of seed solution was mixed with 0.9 mL of sodium citrate and 0.9 mL of $HAuCl_4$ (1 wt%) in 53 mL of water, stirred for 8 min, and then 1.4 mL of hydroxylamine hydrochloride (10 mM) was slowly introduced. The mixture was refluxed for 5 min and stirred at room temperature for 1 h. Polymer coating was performed by polymerizing a mixture of styrene (0.95 mL), divinylbenzene (0.05 mL), and vinylpyrrolidone (300 mg) in 19.5 mL of water and 82.5 mL of ethanol at 70 °C under nitrogen. After 1 h of pre-polymerization, 3 mL of 2,2-azobis (2-methylpropyl) dihydrochloride aqueous solution (1.7 wt%) was added and stirred for 8 min. Next, 15 mL of the gold nanosphere solution was introduced, and the polymerization was continued at 70 °C under nitrogen for 18 h. The resulting AuPS-NPs were collected by centrifugation and washed five times with deionized water to remove unreacted monomers and residual reagents. The morphology and size of PS-NPs and AuPS-NPs were evaluated using TEM. A 2-μL aliquot was deposited onto a carbon-coated film, dried, and imaged using a JEM-1400 TEM (JEOL, Tokyo, Japan).

## Cell Culture

The human gastric adenocarcinoma cell line AGS was obtained from Fenghui Biotechnology Co., Ltd. (Hunan, China), and the human colon adenocarcinoma cell line Caco-2 was purchased from Pricella Biotechnology Co., Ltd. (Wuhan, China). AGS cells were cultured in Minimum Essential Medium (MEM) supplemented with 10% fetal bovine serum (FBS), and Caco-2 cells in MEM containing 20% FBS. Both media also contained 1% penicillin–streptomycin solution. Cells were incubated at 37 °C in a humidified atmosphere of 5% $CO_2$ and 95% air.

## Animal Model Establishment and Sampling

Specific pathogen-free (SPF) male BALB/c mice (5 weeks old, 15–20 g) were obtained from Jinan Pengyue Laboratory Animal Breeding Co., Ltd. (Jinan, China; license number: SCXK Lu 20190003). In this study, sex was defined based on biological attributes, and male mice were used for all experiments. Mice were housed in a controlled environment with 12-h/12-h light/dark cycles, with a temperature of 22 ± 1 °C and a relative humidity of 40–60%. After a 1-week acclimation, 126 mice were randomly assigned (n = 42 per group) into three groups using a random number table: a blank group, a low-dose AuPS-NP group (1 mg/L), and a high-dose AuPS-NP group (10 mg/L). Mice in the blank group received intragastric administration of 0.2 mL of saline, while mice in the exposure groups were gavaged daily with 0.2 mL of AuPS-NPs at concentrations of 1 mg/L or 10 mg/L for 98 consecutive days. Mice were euthanized via intraperitoneal injection of pentobarbital sodium on days 1, 7, 14, 28, 42, 70, and 98 after exposure initiation (n = 6 per group at each time point). Gastric, intestinal, and hepatic tissues were harvested for downstream analyses. These data were subsequently incorporated into TK-TD modeling for quantitative human health risk assessment.

## Cell Viability Assay

Cell viability was evaluated using the cell counting kit-8 (CCK-8) assay (Beyotime Biotechnology, Shanghai, China). AGS and Caco-2 cells were seeded into 96-well plates at a density of $3\times10^3$ cells/well and incubated at 37 °C to allow for adhesion to the substrate. Blank wells (medium only), control wells (untreated cells), and treatment wells (cells exposed

to NPs) were included. After adherence, culture media were removed and cells were rinsed twice with phosphate-buffered saline (PBS, Meilunbio, Dalian, China). Cells were then treated with PS-NP or AuPS-NP suspensions at concentrations of 1 or 10 mg/L, diluted in Optimized Minimum Essential Medium (Opti-MEM; Thermo Fisher Scientific, Waltham, MA, USA), and incubated for the indicated time periods.

After treatment, nanoplastic-containing media were removed, and cells were again rinsed with PBS. Next, 100 μL of fresh culture medium containing 10% (v/v) CCK-8 solution was added to each well. To prevent edge effect and evaporation, PBS was added to the perimeter wells. After 2 h of incubation at 37 °C, the absorbance at 450 nm was measured using a microplate reader (Infinite M200 PRO, Thermo Fisher Scientific). Cell viability was calculated as follows:

$$\text{Cell viability}(\%) = \frac{OD_{treatment} - OD_{blank}}{OD_{control} - OD_{blank}} \times 100\%.$$

## Cellular Reactive Oxygen Species (ROS) Measurement

Intracellular ROS levels were measured using an ROS assay kit (Solarbio, Beijing, China) according to the manufacturer's instructions. AGS and Caco-2 cells were seeded into 6-well plates at a seeding density of $3\times10^5$ cells/well and incubated at 37 °C to allow for adhesion to the substrate. Cells were randomly assigned into blank, positive control, and experimental groups. After adherence, cells were washed twice with PBS and treated with PS-NPs or AuPS-NPs at concentrations of 1 and 10 mg/L, diluted in Opti-MEM. After exposure for the indicated time, the nanoplastic-containing medium was removed, and cells were rinsed twice with PBS.

For the positive control group, ROSup solution (provided in the kit) was added and incubated for 20 min at 37 °C to induce ROS generation. After removing ROSup solution, all wells were washed three times with PBS, followed by incubation with 2′,7′-dichlorodihydrofluorescein diacetate (DCFH-DA) working solution (ROS probe) at 37 °C for 30 min in the dark. After staining, cells were washed three times with serum-free medium to remove excess dye. Finally, 1 mL of PBS was added to each well, and the fluorescence intensity was measured using a microplate reader at an excitation/emission wavelength of 488/525 nm.

## Assessment of Mitochondrial Membrane Potential (Δψm)

Δψm was evaluated using a 5,5′,6,6′-tetrachloro-1,1′,3,3′-tetraethylbenzimidazolylcarbocyanine iodide (JC-1) assay kit (M8650, Solarbio) according to the manufacturer's instructions. AGS and Caco-2 cells were seeded at a density of $1\times10^5$ cells/well into laser confocal culture dishes (Lanjieke, Beijing, China) and incubated at 37 °C for adhesion to the substrate. Cells were randomly divided into blank, positive control, and experimental groups. After adherence, cells were rinsed twice with PBS, and PS-NPs or AuPS-NPs at concentrations of 1 or 10 mg/L were added in Opti-MEM and incubated for the indicated time periods.

After exposure, the nanoplastic suspensions were removed, and cells were washed twice with PBS. For the positive control group, carbonyl cyanide m-chlorophenyl hydrazone (CCCP) working solution was added to depolarize the mitochondrial membrane for 20 min at 37 °C. All wells were then washed once with PBS, followed by the addition of 1 mL of JC-1 working solution and 1 mL of serum-free medium. Cells were incubated at 37 °C for 20 min in the dark. After staining, the supernatant was removed on ice, and cells were washed twice with JC-1 staining buffer (1×). Finally, 2 mL of serum-free medium was added to each dish, and the cells were immediately observed using a laser scanning confocal microscope (Olympus, Tokyo, Japan). Fluorescence intensities were measured from three randomly selected independent microscopic fields. The relative mitochondrial membrane potential was calculated as follows:

$$Relative\,\Delta\psi\text{m} = \frac{\text{Red/Green fluorescence ratio of experimental group}}{\text{Red/Green fluorescence ratio of blank group}}.$$

## Quantification of AuPS-NPs in Tissues by ICP-MS

The accumulation of AuPS-NPs in mouse tissues was quantified by measuring Au content using ICP-MS (Thermo Fisher Scientific). In brief, collected tissues were weighed and transferred to microwave digestion vessels. Each sample was first pre-digested with 5 mL of ultrapure $HNO_3$ and incrementally heated at 70 °C until the tissue was fully dissolved. After

cooling to room temperature, 2 mL of $HNO_3$ and 2 mL of ultrapure $H_2O_2$ were added to the vessels. Microwave digestion was then performed under a temperature program (Supplementary Table S1).

After digestion, vessels were cooled to room temperature before opening. Residual liquid was evaporated to 5–6 mL at 120 °C before final dilution. The digests were then cooled again and brought to a final volume of 25 mL with ultrapure water.

Standard Au solutions were prepared by serial dilution of a gold stock solution using nitric acid. After optimizing instrument conditions, gold concentrations in digested tissues were measured by ICP-MS. The nitric-acid digestion method used in this study follows previously established and widely validated protocols for gold quantification in biological tissues. This procedure provides an acceptable recovery range of 80–120%, supporting the reliability of our quantitative results.[24–27] The number of AuPS-NP particles ($N$) was calculated based on the total gold content in each tissue sample, assuming spherical gold cores and neglecting the polystyrene shell thickness. The formula used was:

$$N = \frac{C_{\mathrm{Au}}}{\frac{4}{3}\pi r^3 \rho_{\mathrm{Au}}},$$

where $C_{\mathrm{Au}}$ is the gold concentration (ng/g·bw), $r$ is the radius of the gold core (cm), and $\rho_{\mathrm{Au}} = 19.32\ \mathrm{g/cm^3}$ is the density of gold.

## Transmission Electron Microscopy (TEM) Sample Preparation

Intestinal tissues were collected immediately after euthanasia and fixed in 2.5% glutaraldehyde at 4 °C overnight. After rinsing with 0.1 mol/L PBS, samples were post-fixed with 1% osmium tetroxide at 4 °C for 90 min with intermittent shaking, dehydrated through a graded ethanol and acetone series, and embedded in epoxy resin (SPI Supplies, West Chester, PA, USA). Ultrathin sections (50–60 nm) were cut using an ultramicrotome (Leica, Wetzlar, Germany), stained with uranyl acetate and lead citrate, and imaged using a Hitachi HT-7800 transmission electron microscope (Hitachi High-Technologies Corporation, Tokyo, Japan).

## Organ Index

Mice were weighed and euthanized, after which major organs, including the stomach, intestine, and liver, were carefully dissected on ice. Fascia and surrounding connective tissues were removed, and residual surface moisture was gently blotted using filter paper. Each organ was then weighed immediately. The organ index was calculated using the following formula:

$$Organ\ index\ (\%) = \frac{Organ\ weight\ (\mathrm{mg})}{Body\ weight\ (\mathrm{g})} \times 100\%.$$

## Detection of Biomarkers via Enzyme-Linked Immunosorbent Assay (ELISA)

The concentrations of TG, T-CHO, ATP, LDH, MDA, SOD, IL-6, and TNF-α in mouse tissues (n = 3) were determined using commercial ELISA kits (Adanti, Wuhan, China). In brief, tissue samples were fully homogenized in PBS, pH 7.4 (1:9 w/v), then centrifuged at 3000 ×g for 20 min at 4 °C, and the supernatants were collected. Aliquots were added to microplates pre-coated with specific capture antibodies for each analyte, followed by enzyme-conjugated reagents. After sequential incubation, washing, and color development, the absorbance at 450 nm was measured using a microplate reader. The concentrations of TG, T-CHO, ATP, LDH, MDA, SOD, IL-6, and TNF-α were calculated according to the corresponding standard curves.

## Establishment of Toxicokinetic–Toxicodynamic (TK–TD) Models

A one-compartment first-order toxicokinetics (TK) model was employed to describe the dynamic interactions between physicochemical agents and biological systems. The modeling strategy was adapted from the framework proposed by Deng et al and modified according to our experimental design.[23] Based on the experimental data, a pulse exposure function incorporating a unit step function (U) was introduced to estimate the time-dependent concentration of AuPS-NPs in specific mouse organs under prolonged oral administration. The analytical expression used for TK fitting is given below:

$$C_i(t) = C_1 \cdot k_1 \cdot e^{k_2 - k_2 t} \sum_{n=1}^{t} e^{(n-1)k_2} \mathrm{U}(-n+t),$$

where *C(t)* is the time-dependent concentration of AuPS-NPs in organ (μg/g·bw), $C_1$ is the input concentration (set according to exposure group: 0, 1, or 10 mg/L), $k_1$ is the uptake rate constant of AuPS-NPs in mice (mL/g/day), $k_2$ is the elimination rate constant of AuPS-NPs from the specific organ (1/day), $t$ is the exposure time (day) and n is the pulsed frequency. Subsequently, when the interaction between AuPS-NPs and intestinal tissue reaches a steady state, the BCFss at steady state can be calculated based on the TK parameters as follows:

$$\mathrm{BCF_{ss}} = \frac{C_i}{C_w} = \frac{k_1}{k_2},$$

where $C_w$ represents the concentration of AuPS-NPs in the exposure solution (mg/L).

For the toxicodynamics (TD) modeling, the relationship between the concentration of AuPS-NPs in the intestinal tissue and the biological response was fitted using the Hill equation:

$$E(C_L) = \frac{E_{max} \cdot C_L^{n_H}}{EC50^{n_H} + C_L^{n_H}},$$

where $E$ represents the change in biological marker effects, including IL-6, TG, LDH, and MDA in mouse intestinal tissue (%), $C_L$ refers to the intermediate concentration of AuPS-NPs in the mouse intestine (μg/g·bw), $E_{max}$ is the maximum effect (%), $EC50$ is the concentration of AuPS-NPs that induces half of the maximum effect (μg/g·bw), and $n_H$ is the Hill coefficient, which represents the slope of the dose-response model.

## Predictive Risk Threshold and Extrapolation Algorithm

The three-parameter Weibull threshold model was used to fit the percentile values (2.5, 5, 25, 50, 75, 95, and 97.5) extracted from the $EC50$ cumulative density function. The risk threshold model was expressed as:

$$F(C_L) = 1 - \exp\left[-\left(\frac{C_L - \gamma}{\alpha}\right)^{\beta}\right], C_L > \gamma > 0, \alpha > 0, \beta > 0,$$

where $F(C_L)$ is the cumulative probability, which is the proportion of effects occurring at a given concentration $C_L$,$\alpha$ is the scale parameter, $\beta$ is the shape parameter, and $\gamma$ is the threshold value (μg/g·bw).

The threshold dose of mouse biomarkers estimated by the Weibull model replaces the no observed adverse effect level (NOAEL), and the human equivalent dose (HED) of AuPS-NPs are derived based on the reference body weights of mice ($W_{\mathrm{mice}}$; 0.02 kg) and humans ($W_{\mathrm{human}}$; 60 kg), as well as the allometric exponent (b):

$$\mathrm{HED} = \mathrm{NOAEL_{mouse}} \cdot \left(\frac{W_{\mathrm{mouse}}}{W_{\mathrm{human}}}\right)^{(1-b)}.$$

The HEDs value was further divided by the historically standard default safety factor of 10. The HEDs was then converted into the threshold number of AuPS-NP particles that would induce toxicity in humans based on the AuPS particle number (N) formula.

## Statistical Analysis

All statistical analyses were performed using statistical package for the social sciences (SPSS) software (version 22.0; IBM, Armonk, NY, USA). Data are presented as mean ± standard deviation (SD). Normality and homogeneity of variances were verified prior to statistical testing. Comparisons between two groups were conducted using independent-samples *t* tests, while comparisons among three or more groups were assessed by one-way analysis of variance (ANOVA), followed by Tukey's post hoc multiple-comparison test to determine pairwise differences. Two-way repeated measures ANOVA was used to evaluate differences over time and treatment, followed by Bonferroni-adjusted post hoc comparisons. Statistical significance was set at $P < 0.05$. Ordinary differential equations (ODEs) used in the TK modeling were solved using Mathematica software

(version 11.2; Wolfram Research, Champaign, IL, USA). Graphs were generated using Prism 8 (GraphPad Software, San Diego, CA, USA) and Photoshop 2020 (Adobe Systems, San Jose, CA, USA).

Other detailed methods are available in the Supplementary Material: Supplementary Methods.

# Results

## Characterization and Size Uniformity of PS-NPs and AuPS-NPs

TEM was used to examine the morphology of PS-NPs and AuPS-NPs. PS-NPs appeared as uniform, smooth-surfaced spheres (Figure 1A and B), whereas AuPS-NPs exhibited a similar spherical shape (Figure 1C and D), with a polystyrene shell evenly encapsulating the gold core. Particle size analysis revealed that the average diameter of PS-NPs was 99.05 ± 5.33 nm, while that of AuPS-NPs measured 101.22 ± 10.43 nm (Figure 1E). These results confirm the successful construction of AuPS-NPs with a polystyrene-coated gold core and demonstrate that both nanoparticle types possess comparable surface morphology. The absence of a statistically significant difference in particle size further supports their structural equivalence, validating their use in subsequent biodistribution and toxicity evaluations.

Fourier-transform infrared spectroscopy (FTIR) spectra further confirmed that both PS-NPs and AuPS-NPs exhibited the characteristic absorption peaks of polystyrene (Figure 1F). The bands at 3020–3080 $cm^{-1}$ correspond to aromatic C–H stretching, while the peaks at 1600, 1490, and 1450 $cm^{-1}$ arise from benzene ring skeletal vibrations. Additionally, the strong out-of-plane C–H bending signals at approximately 750 and 700 $cm^{-1}$ are typical fingerprint features of polystyrene. The

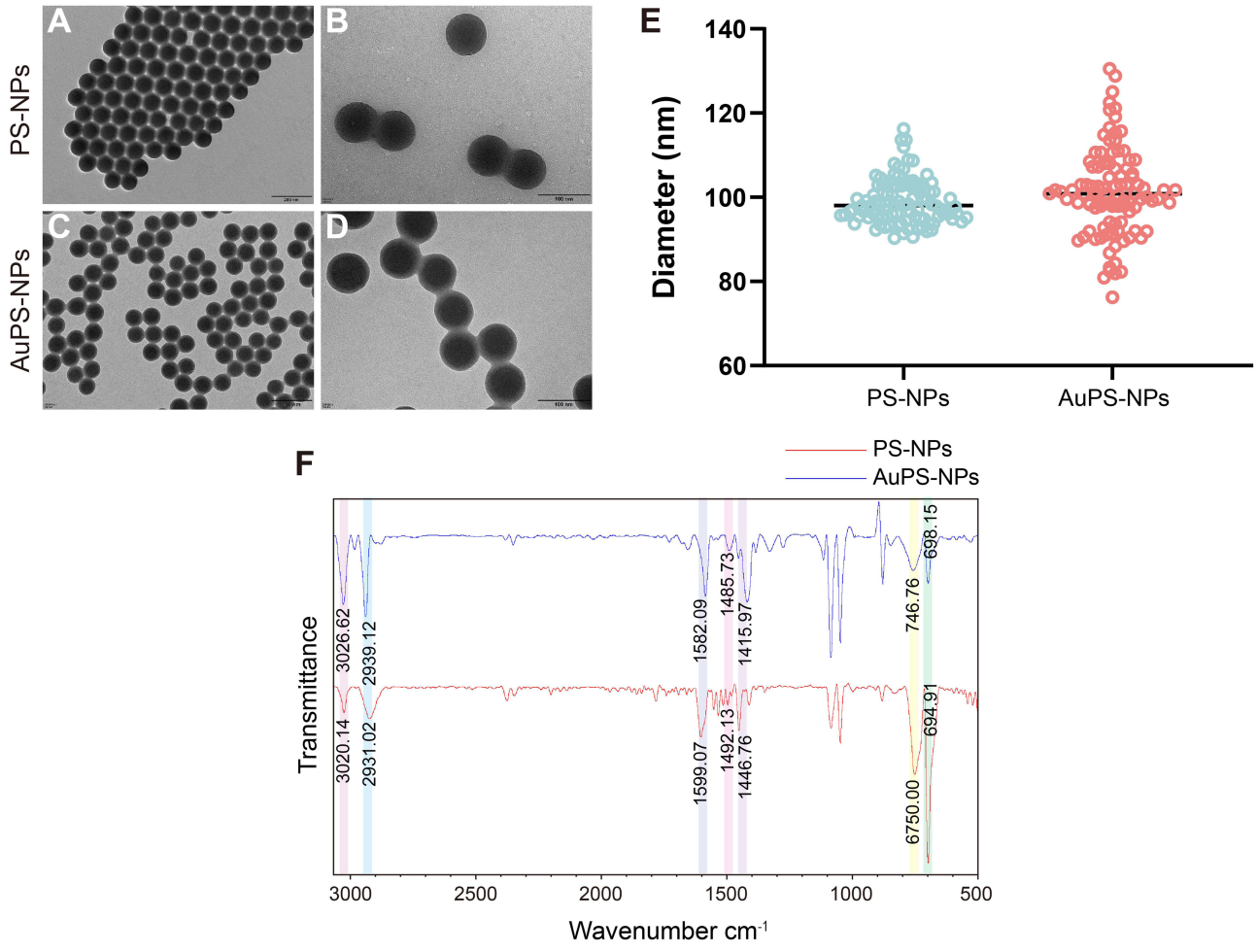


**Figure 1** TEM characterization, particle size distribution, and FTIR analysis of PS-NPs and AuPS-NPs. (**A–D**) TEM images showing the uniform spherical morphology of PS-NPs and AuPS-NPs. Scale bars: 200 nm (**A and C**) and 100 nm (**B** and **D**). (**E**) Particle size distribution analysis of PS-NPs and AuPS-NPs based on measurements from TEM images. (**F**) FTIR spectra of PS-NPs and AuPS-NPs.


https://doi.org/10.2147/IJN.S567996

presence of these identical characteristic peaks in AuPS-NPs demonstrates that the gold core is uniformly coated with a polystyrene shell, and that the surface chemical structure remains consistent with that of pure PS-NPs. Zeta potential measurements showed that both PS-NPs and AuPS-NPs exhibited similarly negative surface charges, indicating good colloidal stability (Figure S1A and B). In addition, dynamic light scattering (DLS) analysis revealed narrow and monodisperse hydrodynamic size distributions for both types of nanoparticles (Figure S1C and D), supporting their good dispersion behavior and confirming that the synthesized nanomaterials possess stable and uniform structural characteristics.

## AuPS-NPs Exhibit Equivalent Cytotoxicity to PS-NPs

To exclude potential cytotoxic effects from the exposed gold core of the synthesized material and to evaluate the toxicological equivalence of AuPS-NPs and PS-NPs, cytotoxicity assays were performed using gastrointestinal epithelial cell lines AGS and Caco-2. Cell viability was measured using the CCK-8 assay following 12 h and 24 h exposures to PS-NPs and AuPS-NPs at concentrations of 0, 1, and 10 mg/L. In AGS cells, significant reductions in viability were observed at 24 h (1 mg/L) and 12 h (10 mg/L; $P < 0.05$). Specifically, PS-NPs decreased viability by 6.11% and 12.46% at the respective concentrations (Figure 2A), while AuPS-NPs caused reductions of 6.88% and 12.89% (Figure 2B). These results demonstrate a time- and concentration-dependent decrease in cell viability for both NPs types (Figure 2A–D). A similar pattern was observed in Caco-2 cells, confirming the reproducibility of the cytotoxic response (Figure 2E–H).

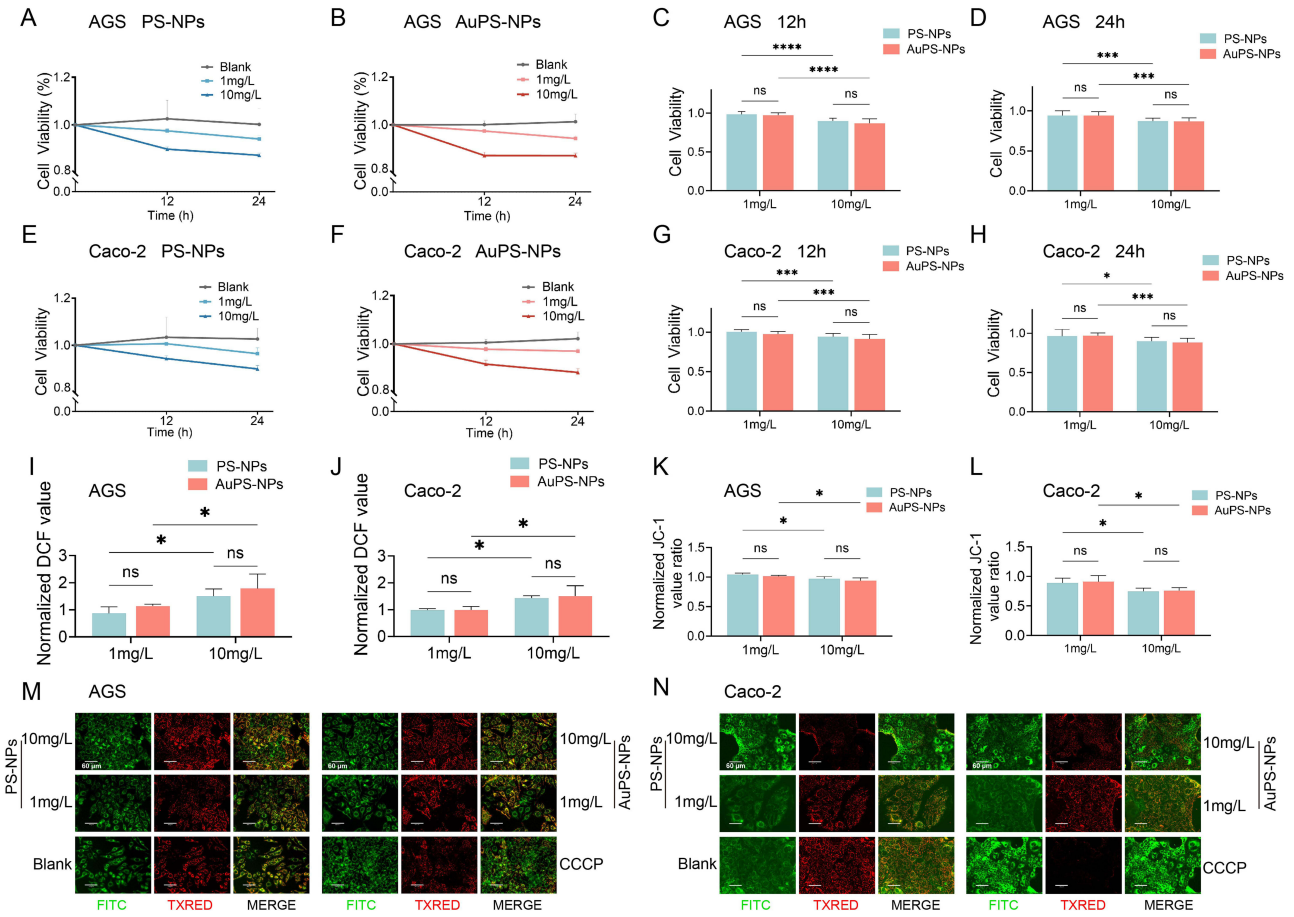


**Figure 2** PS-NPs and AuPS-NPs induced comparable cytotoxicity in cells. (**A** and **B**) Cell viability of AGS cells exposed to PS-NPs (**A**) or AuPS-NPs (**B**) at 0, 1 and 10 mg/L for 12 h and 24 h, measured by CCK-8 assay (n = 3). (**C** and **D**) Quantification of AGS cell viability at 12 h (**C**) and 24 h (**D**) (n = 3). (**E** and **F**) Cell viability of Caco-2 cells exposed to PS-NPs (**E**) or AuPS-NPs (**F**) (n = 3). (**G** and **H**) Quantification of Caco-2 cell viability at 12 h (**G**) and 24 h (**H**) (n = 3). (**I** and **J**) Intracellular ROS levels in AGS cells (**I**) and Caco-2 cells (**J**) after 24 h exposure to PS-NPs or AuPS-NPs, measured based on 2′,7′-dichlorofluorescein (DCF) fluorescence intensity (n = 3). (**K** and **L**) Relative ΔΨm in AGS cells (**K**) and Caco-2 cells (**L**) after 24 hours of exposure to PS-NPs or AuPS-NPs. (**M** and **N**) Representative JC-1 fluorescence images in AGS cells (**M**) and Caco-2 cells (N). Red fluorescence indicates JC-1 aggregates in cells with intact ΔΨm, while green fluorescence indicates JC-1 monomers in depolarized mitochondria. Relative ΔΨm was calculated based on the red/green fluorescence ratio. CCCP was used as a positive control. Scale bars: 60 μm. Data are presented as mean ± SD, ns: not significant; *$P < 0.05$; ***$P < 0.001$; ****$P < 0.0001$.

Given the known role of oxidative stress in NPs cytotoxicity, intracellular ROS levels were measured. After 24 h of exposure, both PS-NPs and AuPS-NPs led to an increase in ROS production, with significantly higher levels observed in the 10 mg/L group compared to the 1 mg/L group ($P < 0.05$). In AGS cells, ROS levels in the 10 mg/L group were elevated by 1.73-fold and 1.57-fold for PS-NPs and AuPS-NPs, respectively, compared to the 1 mg/L group (Figure 2I). Similarly, in Caco-2 cells, ROS levels increased by 1.47-fold and 1.52-fold, respectively (Figure 2J).

Because excessive ROS can disrupt mitochondrial function, ΔΨm was assessed using JC-1 staining. In untreated control cells with high ΔΨm, JC-1 aggregated in the mitochondrial matrix and emitted red fluorescence. In cells with low ΔΨm, JC-1 existed as a monomer and emitted green fluorescence.[28] Following 24 h of exposure to either PS-NPs or AuPS-NPs, a decrease in red fluorescence intensity and an increase in green fluorescence intensity were observed, indicating mitochondrial depolarization (Figure 2M and N). The red/green fluorescence ratio between experimental and blank groups was used to quantify the relative ΔΨm, reflecting the extent of mitochondrial depolarization. In Caco-2 cells, exposure to 10 mg/L of PS-NPs or AuPS-NPs reduced the relative ΔΨm to 0.75 ± 0.05 and 0.76 ± 0.05, respectively, corresponding to a 14% and 15% reduction compared to the 1 mg/L group (Figure 2L). A similar trend was observed in AGS cells, where the 10 mg/L group showed decreases of 8% and 7% in the relative ΔΨm compared to the 1 mg/L group (Figure 2K).

Importantly, PS-NPs and AuPS-NPs demonstrated consistent toxicological profiles across all assays, including CCK-8 (Figure 2C–H), ROS (Figure 2I and J), and JC-1 (Figure 2K and L). No statistically significant differences were observed between the two NP types at corresponding concentrations and durations ($P > 0.05$), supporting the use of AuPS-NPs as a suitable surrogate for conventional PS-NPs in in vitro toxicity assessments.

## Time- and Dose-Dependent Accumulation of AuPS-NPs in Intestinal Tissue

TEM revealed the presence of AuPS-NPs in intestinal tissues of mice exposed to 1 mg/L and 10 mg/L AuPS-NPs, whereas no particles were observed in the blank group (Figure 3A). To quantify accumulation, gold content in intestinal tissues was measured by ICP-MS over a 98-day exposure period (Figure 3B). AuPS-NPs levels in the intestinal tissues of the blank group remained low and relatively stable, while the 1 mg/L and 10 mg/L groups showed progressive, dose-dependent increases. In the 10 mg/L group, gold accumulation increased from 1.31 ± 0.65 ng/g on day 1 to 8.43 ± 0.07 ng/g on day 98. Similarly, in the 1 mg/L group, levels increased from 1.66 ± 0.18 ng/g to 3.77 ± 0.60 ng/g over the same period. One-way ANOVA confirmed that the AuPS-NPs concentration significantly affected accumulation ($F = 449.48$, $P < 0.001$), while exposure duration also had a significant impact ($F = 45.77$, $P < 0.001$), with accumulation increasing consistently over time. Two-way repeated measures ANOVA revealed a significant group × time interaction, indicating that the rate of AuPS-NPs accumulation differed among the dosage groups. Post-hoc pairwise comparisons showed that both exposure groups had significantly higher levels of intestinal AuPS-NPs accumulation compared to the blank group ($P < 0.05$). By contrast, the 10 mg/L group accumulated significantly more than the 1 mg/L group ($P < 0.05$). These findings indicate a clear time- and dose-dependent accumulation of

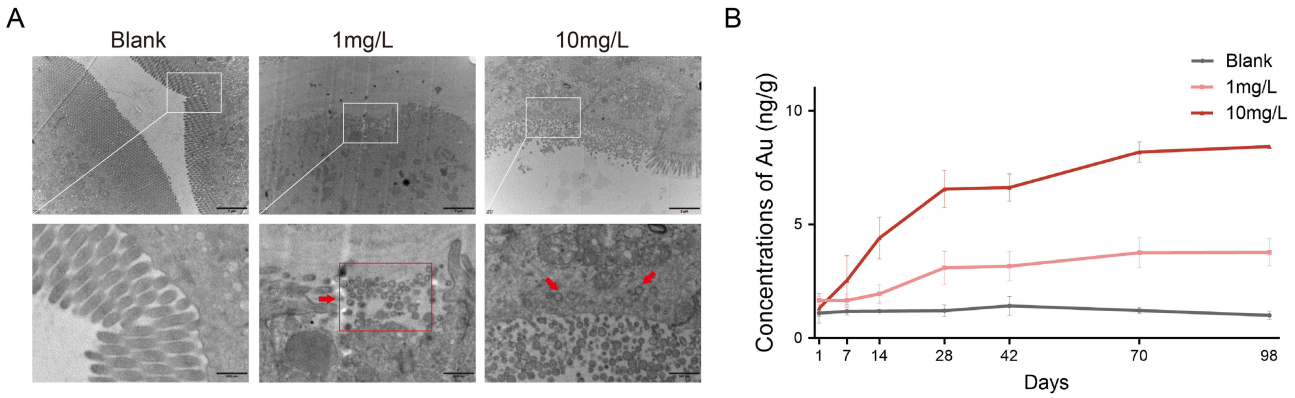


**Figure 3** Accumulation of AuPS-NPs in intestinal tissues following long-term exposure. (**A**) TEM images showing the presence of AuPS-NPs (red arrows) in intestinal tissue on day 98. Scale bars: 2 μm and 500 nm. (**B**) Elemental gold Au accumulation in intestinal tissues was quantified by ICP-MS over time at different exposure concentrations. Data are presented as mean ± SD (n = 3).


https://doi.org/10.2147/IJN.S567996

AuPS-NPs in intestinal tissue, supporting their persistence and progressive retention under environmentally relevant exposure conditions. In addition to intestinal tissues, we further evaluated the biodistribution of AuPS-NPs in other major organs. ICP-MS analysis revealed detectable gold accumulation in both the liver and stomach at day 98, with a pronounced dose-dependent increase (Figure S3A and B). These results indicate that AuPS-NPs are not confined to the intestine but can undergo multi-organ bioaccumulation during long-term exposure.

## Long-Term Exposure to AuPS-NPs Decreases Body Weight and Increases Organ Indices

To evaluate the systemic effects of prolonged AuPS-NPs exposure, body weight and organ indices were monitored to assess potential systemic effects of long-term exposure. No significant differences in body weight were observed among groups during the early phase. However, from day 28 onward, mice exposed to 1 mg/L and 10 mg/L AuPS-NPs exhibited significantly lower body weights compared to the blank group ($P < 0.01$), and the 10 mg/L group also showed significantly lower body weights than the 1 mg/L group ($P < 0.001$). By day 98, the mean body weights of mice in the 1 mg/L (28.95 ± 0.66 g) and 10 mg/L (28.46 ± 0.86 g) groups had decreased by 7.96% and 9.52%, respectively, compared to the blank group (31.46 ± 1.52 g; Figure 4A).

Organ indices were subsequently determined to evaluate whether AuPS-NPs exposure affected specific organs. The gastric index increased significantly in the 1 mg/L and 10 mg/L groups compared to the blank group beginning on day 14 ($P < 0.05$), with the 10 mg/L group also exceeding the 1 mg/L group after day 28 ($P < 0.01$; Figure 4B). Similar trends were observed for intestinal and hepatic indices, with increases in the 1 mg/L and 10 mg/L groups detected on day 7 and 14, respectively (Figure 4C and D). By day 98, the gastric, intestinal, and hepatic indices in the 1 mg/L group had increased by 10.82%, 15.41%, and 12.38% compared to the blank group, while the 10 mg/L group showed increases of 24.16%, 24.64%, and 22.56%, respectively. These findings suggest that long-term exposure to AuPS-NPs results in sustained body weight loss and dose-dependent increases in gastric, intestinal, and hepatic indices, suggesting physiological disturbances.

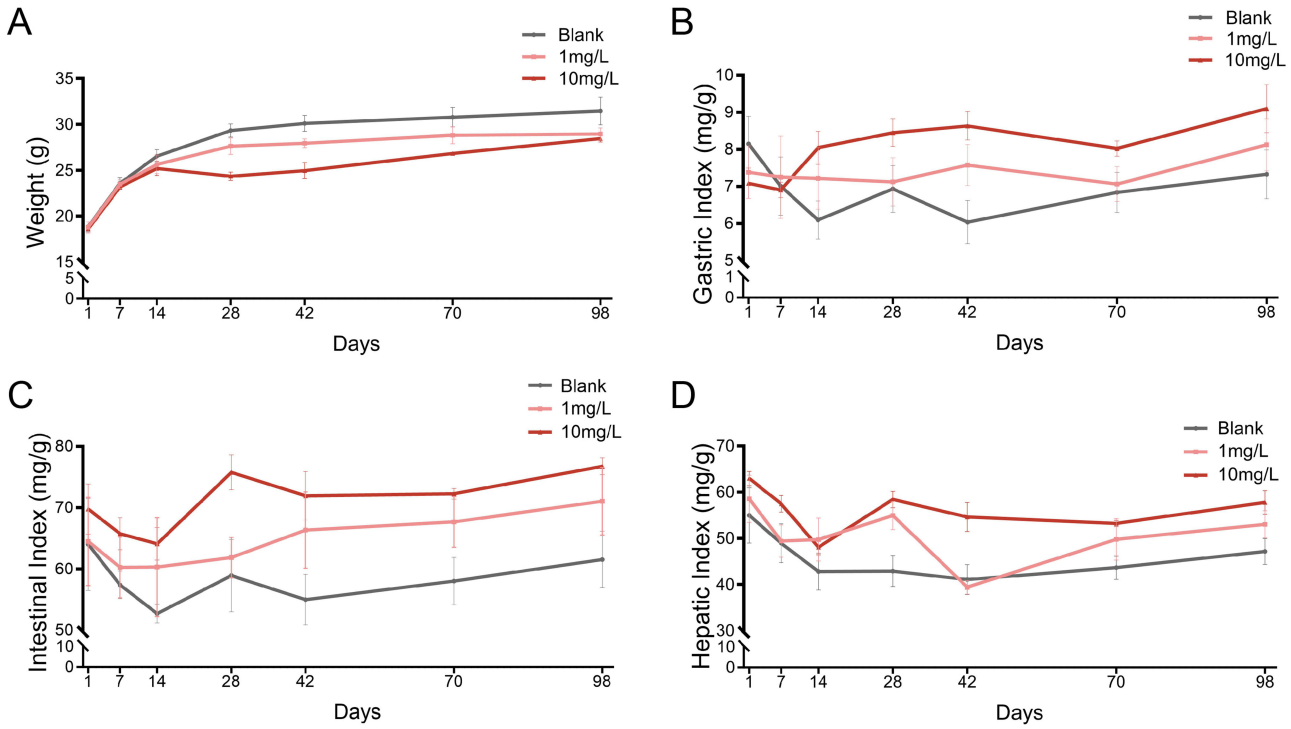


**Figure 4** Effects of long-term AuPS-NPs exposure on body weight and organ indices in mice. (**A**) Changes in body weight over a 98-day exposure period. (**B**–**D**) Temporal trends in gastric (**B**), intestinal (**C**), and hepatic (**D**) indices (mg/g) in the blank, 1 mg/L, and 10 mg/L exposure groups. Data are presented as mean ± SD (n = 6).

## Long-Term Exposure to AuPS-NPs Elicits Systemic Inflammatory, Oxidative, Energetic, and Lipid Metabolic Disturbances

Given that inflammation is an early response to xenobiotic exposure, proinflammatory cytokines IL-6 and TNF-α were initially quantified (Figure 5A and B). Both markers showed significant time- and dose-dependent increases ($P < 0.05$). By day 98, IL-6 levels in the 10 mg/L group significantly increased to 157.25 ± 1.91 pg/mL (stomach), 164.35 ± 2.70 pg/mL (intestine), and 164.24 ± 1.39 pg/mL (liver), corresponding to 1.82-, 2.56-, and 2.43-fold increases versus the blank group, respectively. The 1 mg/L group also exhibited significant increases of 1.54-, 2.02-, and 2.30-fold, respectively. Similar dose-dependent trends were observed for TNF-α (1.80–2.09-fold). These results indicate a progressive inflammatory response that intensified with dose and duration.

Given the association between inflammation and oxidative stress, MDA and SOD were measured as indicators of lipid peroxidation and antioxidant defense, respectively (Figure 5C and D). As a terminal product of lipid peroxidation, MDA was significantly elevated in both exposure groups ($P < 0.05$). At the end of the 98-day exposure period, MDA levels in the 1 mg/L group were 1.66-, 1.64-, and 1.67-fold higher than the blank group in gastric, intestinal, and hepatic tissues, respectively. The 10 mg/L group showed even more pronounced increases of 2.24-, 1.88-, and 2.34-fold. By contrast, SOD, a key indicator of antioxidant defense, significantly decreased ($P < 0.05$), with reductions of 39.63%, 34.10%, and 33.03% in the 1 mg/L group and 48.73%, 54.47%, and 54.29% in the 10 mg/L group across the same tissues. These changes reflect an imbalance in oxidative homeostasis, characterized by elevated oxidative damage and impaired antioxidant capacity.

To further evaluate the physiological consequences of oxidative stress, markers of energy metabolism ATP and LDH were measured (Figure 5E and F). By day 98, ATP levels significantly decreased in a dose-dependent manner across all tissues ($P < 0.05$). In the 1 mg/L group, ATP levels dropped by 16.97% in the stomach, 31.15% in the intestine, and 16.64% in the liver compared to the blank group. The 10 mg/L group showed sharper declines of 35.75%, 35.33%, and 39.59%. By contrast, LDH levels, which are indicative of cell injury and anaerobic glycolysis, were significantly elevated ($P < 0.05$). The 1 mg/L group exhibited 1.45-, 1.71-, and 1.49-fold increases, while the 10 mg/L group showed greater

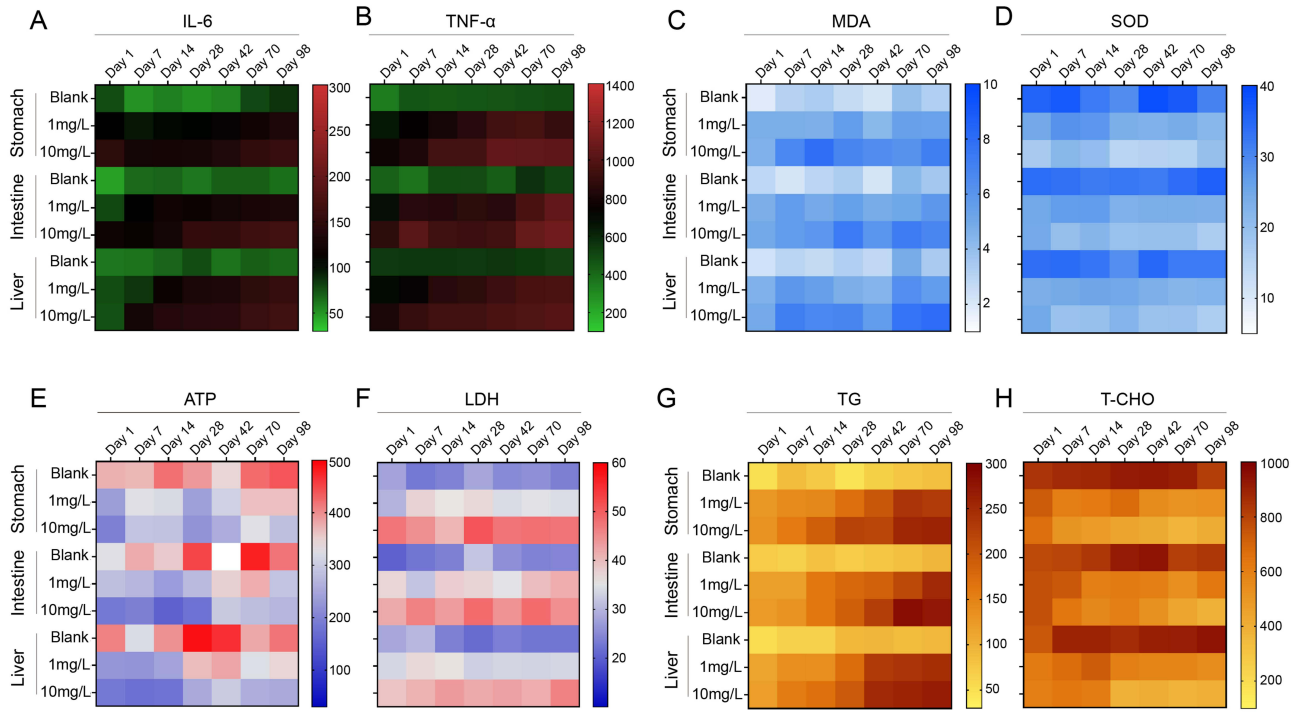


**Figure 5** Heatmap visualization of physiological biomarker alterations in gastric, intestinal, and hepatic tissues following long-term AuPS-NPs exposure in mice (n = 3). (**A** and **B**) Inflammatory cytokines IL-6 (**A**) and TNF-α (**B**). (**C** and **D**) Oxidative stress markers MDA (C) and SOD (D). (**E** and **F**) Energy metabolism indicators ATP (**E**) and LDH (**F**). (**G** and **H**) Lipid metabolism markers TG (G) and T-CHO (H).


https://doi.org/10.2147/IJN.S567996

increases of 2.02-, 1.85-, and 2.06-fold in the corresponding tissues. The shifts in ATP and LDH levels indicate that mitochondrial function and energy production were adversely affected.

Finally, lipid metabolic disturbances were evaluated after long-term AuPS-NPs exposure (Figure 5G and H). Triglyceride, the primary form of lipid storage, was significantly elevated in the exposure groups ($P < 0.05$), suggesting disrupted lipid homeostasis. By day 98, TG levels increased by 2.64–2.69-fold in the 1 mg/L group and by 2.86–3.03-fold in the 10 mg/L group. Total cholesterol, which reflects cholesterol synthesis, transport, and absorption, decreased sharply ($P < 0.05$). By day 98, T-CHO levels in the 1 mg/L group declined by 35.67%, 28.61%, and 50.72% across the three tissues, while the 10 mg/L group showed even greater reductions of 49.58%, 58.41%, and 61.91%. Together, these findings indicate that cholesterol homeostasis was disrupted. This inverse pattern of TG elevation and T-CHO reduction underscores a profound disruption of lipid metabolic balance after AuPS-NPs exposure.

In addition, to confirm the reliability of the key biomarker measurements, we performed supplemental validation of TNF-α and T-CHO in intestinal tissues from mice exposed for 98 days. Reverse transcription quantitative polymerase chain reaction (RT-qPCR) analysis showed that TNF-α mRNA levels were increased by approximately 1.71-fold and 2.64-fold in the 1 mg/L and 10 mg/L groups, respectively, compared with the blank group (Figure S2A). Consistent with this finding, densitometric analysis of the Western blot bands revealed that TNF-α protein expression increased by approximately 1.94-fold and 3.06-fold in the 1 mg/L and 10 mg/L groups (normalized to GAPDH), displaying a clear dose-dependent pattern (Figure S2B and C). Furthermore, an independent T-CHO colorimetric assay demonstrated that intestinal T-CHO levels decreased by 23.26% and 59.58% in the 1 mg/L and 10 mg/L groups, respectively, relative to the blank group (Figure S2D). The supplemental validation results were consistent in trend with the ELISA data.

## TK-TD Analysis of AuPS-NPs in Mice System

To quantitatively determine the threshold number of plastic particles required to elicit biological responses in intestinal tissues, a TK-TD modeling framework was established based on AuPS-NPs exposure in mice. Initially, a one-compartment first-order TK model was fitted to the exposure data to estimate the key TK parameters ($k_1$ and $k_2$) in the intestines of mice exposed to 1 mg/L or 10 mg/L AuPS-NPs. Notably, both $k_1$ and $k_2$ values were higher in the 1 mg/L group than in the 10 mg/L group. Specifically, in the 1 mg/L group, $k_1$ was 0.00016 ± 0.00009 mL/g/day and $k_2$ was 0.79 ± 0.701/day ($R^2 = 0.930$), whereas in the 10 mg/L group, $k_1$ was 0.00004 ± 0.00001 mL/g/day and $k_2$ was 0.05 ± 0.0081/day ($R^2 = 0.994$). The steady state bioconcentration factor (BCFss) was also calculated based on these parameters. Despite lower kinetic parameters, the 10 mg/L group exhibited a higher BCFss (0.0008) than the 1 mg/L group (0.0002), indicating greater bioaccumulation potential under high-dose exposure.

Subsequently, a three-parameter Hill model was used to characterize the dose–response relationships between intestinal AuPS-NP burden and selected biological marker responses. The Hill model effectively captured the nonlinear relationship ($R^2$ = 0.69–0.82; Figure 6A–D). The maximum response amplitudes ($E_{max}$) of IL-6, TG, LDH, and MDA were 538.25%, 671.60%, 299.17% and 307.55%, respectively. The $EC50$ and $n_H$ values for all four biomarkers were consistent, estimated as 0.01 μg/g·bw and 1, respectively.

## Threshold Estimation and Human Health Risk Projection of AuPS-NPs

Using the Hill-based TD model, threshold concentrations of AuPS-NPs that induced changes in intestinal biomarker levels (IL-6, TG, LDH, and MDA) were estimated. Percentile values derived from the $EC50$ distributions were fitted to a three-parameter Weibull threshold model, exhibiting excellent agreement ($R^2 > 0.99$; Figure 6E–H). The estimated threshold concentration corresponding to a 50% increase in biomarker response was 0.0106 ± 0.0062 μg/g·bw in mice. Using interspecies extrapolation, the corresponding human equivalent dose (HED) for gold in humans was estimated as 0.07554 ng/kg. Based on the known mass and density of gold, the estimated threshold number of 100 nm AuPS-NPs required to elicit toxic responses in humans, such as inflammation and oxidative stress, was $9.529 \times 10^5$ particles/kg.

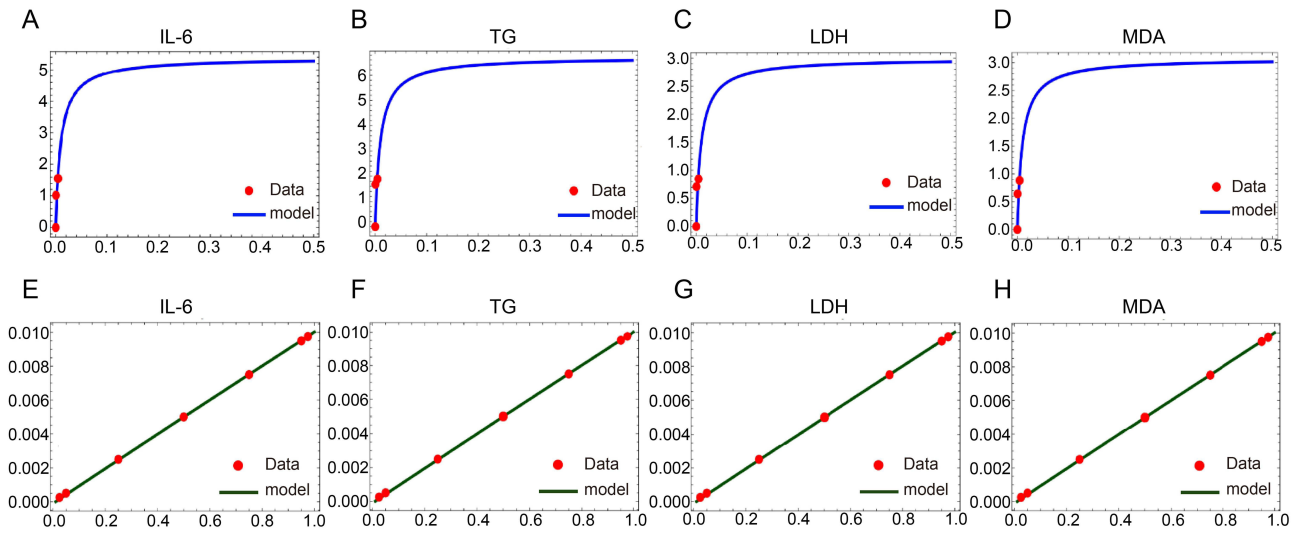


**Figure 6** Dose–response relationships and *EC*50 analysis of AuPS-NPs-induced biological responses in mouse intestinal tissue. (**A–D**) Dose–response curves of IL-6, TG, LDH, and MDA levels in mouse intestinal tissue fitted using the three-parameter Hill-based toxicodynamic model. Red dots represent experimental data; blue curves indicate model predictions. (E–H) Cumulative distribution of *EC*50-derived percentiles modeled using the three-parameter Weibull threshold function. Red dots represent observed cumulative frequencies; green lines indicate the best-fit Weibull model.

## Discussion

NPs have emerged as a new class of environmental pollutants, attracting increasing attention from both the scientific community and the public due to their potential health and ecological impacts.[14,29] Although extensive research exists on the toxicological effects of MPs,[29–31] data on the biological responses to NPs in mammalian systems remain limited.[32] Due to the small size and lack of intrinsic traceability, conventional fluorescent labeling of NPs is prone to quenching and limited accuracy in tissue quantification.[33] Therefore, we engineered AuPS-NPs with an inert gold core and polystyrene shell, enabling precise ICP-MS-based quantitative tracking of particle accumulation. TEM confirmed the successful construction of AuPS-NPs with consistent morphology and size compared to conventional PS-NPs. Comparative analyses using CCK-8, ROS, and JC-1 assays showed that both PS-NPs and AuPS-NPs reduced the viability of AGS and Caco-2 cells, increased ROS production, and mitochondrial membrane depolarization, all of which are hallmarks of oxidative stress and early apoptosis. These results are consistent with prior reports showing that NPs can penetrate cell membranes, cause mitochondrial damage,[10,34] and induce oxidative stress and apoptosis.[35,36] Notably, no significant differences were observed between PS-NPs and AuPS-NPs in terms of cytotoxicity or mitochondrial damage, confirming that AuPS-NPs are excellent surrogates for tracking PS-NPs in the structural stability and toxicological equivalence of AuPS-NPs. These results validate the use of AuPS-NPs as a reliable model for tracking PS-NPs in biological systems.

In vivo experiments further supported the in vitro findings, providing robust evidence for the systemic toxicity of NPs. Long-term oral exposure to AuPS-NPs resulted in progressive accumulation in intestinal tissues, as visualized by TEM and quantified by ICP-MS. In addition, Fourier-transform infrared spectroscopy (FTIR), zeta potential measurements, and particle size distribution analyses further confirmed that AuPS-NPs shared nearly identical surface chemistry, charge characteristics, and dispersion profiles with conventional PS-NPs. Notably, during 98 days of exposure, AuPS-NPs demonstrated remarkable stability, with both ICP-MS and TEM analyses confirming no degradation or leakage of the gold core. This indicates that the polystyrene shell effectively prevented the release of gold ions, ensuring that the observed biological effects were indeed caused by the nanoparticles themselves. Literature reports have shown that polystyrene coatings maintain stability in both acidic and alkaline solutions as well as during long-term storage (up to 180 days), further validating the reliability of AuPS-NPs as a model for chronic exposure risk assessment.[21] The observed accumulation in intestinal tissues may be linked to compromised intestinal barrier function, potentially mediated by downregulation of tight junction proteins (eg Claudin-1) or mucin-related defenses, as observed with long-term exposure to PS-NPs, which caused a significant reduction in Claudin-1 expression and an increase in intestinal permeability after 28 days of exposure.[37] Importantly, body weights of mice decreased


https://doi.org/10.2147/IJN.S567996

significantly in both exposure groups beginning from day 28, which may reflect reduced nutrient absorption caused by epithelial disruption and altered microvilli structure.[38–40] In parallel, disturbances in energy metabolism, as evidenced by ATP depletion and LDH elevation, likely contributed to a negative energy balance.[38] Significant increases in the organ indices of the stomach, intestine, and liver were also observed in the AuPS-NP-exposed mice. While reduced body weight partially explains these increases, the more probable contributing factors are chronic inflammation, organ hypertrophy, and tissue edema. These findings are consistent with previous reports in rodents showing that NPs can cause hepatic lipid accumulation,[41] glycogen storage, hepatocellular edema,[42] and gastrointestinal inflammation.[37,43] This conclusion is further substantiated by the observed changes in downstream biomarkers associated with inflammation, oxidative stress, and metabolic disruption.

Biochemical analyses further highlighted systemic toxicity across multiple physiological domains, characterized by inflammation, oxidative stress, and disrupted energy metabolism. Elevated levels of IL-6 and TNF-α in gastrointestinal and hepatic tissues are indicative of innate immune activation and tissue inflammation, potentially reflecting mucosal barrier disruption and oxidative stress-induced injury.[44] Dysregulation of lipid metabolism is supported by findings showing increased TG and reduced T-CHO levels, implicating impaired lipid synthesis and transport.[45,46] Energy metabolism is also affected: reduced ATP levels point to mitochondrial impairment, which aligns with the mitochondrial dysfunction observed in vitro.[34] Concurrently, elevated LDH levels indicate membrane damage and cytotoxic stress,[47,48] likely resulting from oxidative injury or inflammatory infiltration. Markers of oxidative stress showed similar trends: MDA levels are elevated, reflecting enhanced lipid peroxidation, while SOD activity is suppressed, indicating antioxidant depletion.[49–52] Collectively, these data point to redox imbalance as a central mechanism underlying NP-induced toxicity. Among these biomarkers, TNF-α and T-CHO exhibited the most pronounced and consistent alterations within the inflammatory and metabolic panels, respectively. These characteristics made them suitable representative indicators for additional validation. Supplemental RT-qPCR, Western blot, and colorimetric assays confirmed that their changes were consistent with the ELISA results, further supporting the reliability of our biochemical measurements. These molecular findings underscore the robustness of AuPS-NP-induced toxicity, even at low concentrations.

While some studies report negligible effects of low-dose NPs on aquatic organisms (eg, marine invertebrates with rapid clearance mechanisms), these conclusions are often based on short-term assays or less sensitive detection methods.[53,54] Moreover, extrapolation of such findings to higher organisms with intricate physiological systems may result in an underestimation of potential long-term health risks. In our murine model, ICP-MS-based quantification revealed that even 1 mg/L AuPS-NPs induced progressive intestinal accumulation and various pathophysiological disturbances, highlighting the critical importance of chronic exposure models and advanced analytical tools in risk assessment. It is worth noting that the concentrations used in our study (1 mg/L and 10 mg/L AuPS-NPs) are effectively comparable to 0.1 mg/L and 1 mg/L of PS-NPs, which better reflect environmental exposure levels. This conversion is based on the assumption that AuPS-NPs and PS-NPs share similar toxicological and structural characteristics. By converting the mass of the gold-core polystyrene nanoplastics at the specific concentrations into particle numbers, and further converting these into the concentration of pure polystyrene nanoplastics, we found that the concentrations of AuPS-NPs in our experiments correspond to lower concentrations of pure polystyrene particles. Moreover, previous studies have reported that nanoplastic concentrations in natural freshwater systems typically range from 51 to 563 μg/L, with peak levels in some inland waters reaching 1588 μg/L.[55,56] These concentrations are within the same order of magnitude as the PS-NP–equivalent exposure levels used in this study (0.1 mg/L and 1 mg/L, corresponding to 1 mg/L and 10 mg/L AuPS-NPs). Our prior in vivo work also demonstrated measurable and biologically meaningful tissue accumulation within this dose range.[22] These findings support the environmental relevance and biological justification of the exposure concentrations selected in this study.

Given the complexity of NP-induced systemic toxicity, a quantitative framework linking exposure doses to biomarker responses is critical for risk assessment.[23] Here, we integrated TK-TD modeling to integrate exposure, accumulation, and biomarker response data, enabling extrapolation to human health risk scenarios. The first-order kinetic model provided robust estimates of TK parameters ($k_1$, $k_2$, BCFss). In contrast, the Hill-based TD model accurately described dose–response relationships between intestinal AuPS-NP concentrations and changes in IL-6, TG, LDH, and MDA. A Weibull

cumulative distribution model was fitted to the threshold response data, yielding an estimated human Au threshold level of 0.07554 ng/kg, which corresponds to $9.529\times10^5$ particles/kg of 100 nm AuPS-NPs.

In this study, we present the first reported human toxicity threshold of $9.529\times10^5$ particles/kg for NPs, providing a particle-based benchmark for evaluating chronic NPs exposure risk. This value reflects the particle burden sufficient to elicit redox imbalance, pro-inflammatory cytokine elevation, and metabolic dysregulation in the intestine. Surprisingly, recent studies have reported nanoplastic concentrations in bottled water ranging from $1.1\times10^5$ to $3.7\times10^5$ particles/L, with one high-resolution Raman imaging study identifying an average of $2.4\times10^5$ particles/L, around 90% of which were < 1 μm in diameter.[8,57] Assuming a daily intake of 2L, annual exposure may reach $1.75\times10^8$ particles—already exceeding the modeled threshold for a 70 kg individual.[58] Similarly, plastic particles have been found in seafood (up to 10.5 particles/g) and edible salt (0–1674 particles/kg).[58] These findings suggest that current environmental exposure could cumulatively reach biologically significant levels. While our model adopts conservative interspecies scaling, it does not account for vulnerable populations (eg infants, patients with gut barrier dysfunction), and thus, the actual safety margin may be narrower than expected.

Our study has certain limitations, including the lack of long-term evaluations involving reproductive, neurological, and other systemic outcomes, as well as the absence of sex-specific analyses. Nonetheless, our findings provide strong evidence that prolonged exposure to PS-NPs, even at environmentally relevant concentrations, may pose substantial health risks. The TK-TD modeling and threshold-based extrapolation highlight the need to re-evaluate current regulatory frameworks for NPs. Future studies should focus on the effects of chronic low-dose exposure in vulnerable populations and consider the cumulative impacts of multiple exposure pathways.

## Conclusion

In summary, this study developed AuPS-NPs as a quantifiable surrogate for PS-NPs, enabling precise in vivo tracking of NP biodistribution and toxicity. AuPS-NPs demonstrated toxicological equivalence to PS-NPs in gastrointestinal epithelial cells, validating their use for modeling systemic exposure. In mice, chronic oral administration of AuPS-NPs led to progressive intestinal accumulation, body weight loss, and organ-specific physiological disturbances, accompanied by inflammation, oxidative stress, and metabolic dysregulation. Integrating these findings into a TK-TD framework enabled the estimation of a human toxicity threshold of $9.529\times10^5$ particles/kg, indicating that current environmental exposure levels may approach or exceed this benchmark. This study provides a robust particle-based strategy for assessing NP health risks and highlights the urgency of re-evaluating regulatory standards for emerging nanocontaminants.

## Data Sharing Statement

The data are available from the corresponding author upon reasonable request.

## Ethics Declarations

All animal experimental protocols in this study were approved by the Animal Use and Care Committee of Binzhou Medical University (Approval No. 2022-386) and were conducted in accordance with the Laboratory Animal Environment and Facilities (GB 14925-2010) and the Animal Research: Reporting of In Vivo Experiments (ARRIVE) 2.0 guidelines.

## Acknowledgments

We thank Chung-Min Liao and Chi-Yun Chen from National Taiwan University for their valuable guidance in the establishment of the TK-TD model for this experiment. We thank International Science Editing (http://www.internationalscienceediting.com) for editing this manuscript.

## Author Contributions

All authors made a significant contribution to the work reported, whether that is in the conception, study design, execution, acquisition of data, analysis and interpretation, or in all these areas; took part in drafting, revising or critically

reviewing the article; gave final approval of the version to be published; have agreed on the journal to which the article has been submitted; and agree to be accountable for all aspects of the work.

## Funding

This work was supported by National Natural Science Foundation of China [Grant numbers: 82172560 and 42077402], Taishan Scholar Foundation of Shandong Province, China [Grant numbers: tsqn202211229], Special supporting funds for leading talents above the provincial level in Yantai city, China.

## Disclosure

The authors declare that they have no competing interests.

## References

1. Hu Y, Tian Y, Zou C, Moon TS. The current progress of tandem chemical and biological plastic upcycling. *Biotechnol Adv*. 2024;77:108462. doi:10.1016/j.biotechadv.2024.108462
2. Jambeck JR, Geyer R, Wilcox C, et al. Plastic waste inputs from land into the ocean. *Science*. 2015;347(6223):768–771. doi:10.1126/science.1260352
3. Rasilainen I, Lahtela V, Kärki T. A review of plastic waste nanocomposites: assessment of features and applications. *Discov Nano*. 2024;19(1):112. doi:10.1186/s11671-024-04062-0
4. Lv S, Cui K, Zhao S, et al. Continuous generation and release of microplastics and nanoplastics from polystyrene by plastic-degrading marine bacteria. *J Hazard Mater*. 2024;465:133339. doi:10.1016/j.jhazmat.2023.133339
5. Yang Q, Dai H, Cheng Y, et al. Oral feeding of nanoplastics affects brain function of mice by inducing macrophage IL-1 signal in the intestine. *Cell Rep*. 2023;42(4). doi:10.1016/j.celrep.2023.112346
6. Wang Z, Pal D, Pilechi A, Ariya PA. Nanoplastics in water: artificial intelligence-assisted 4D physicochemical characterization and rapid in situ detection. *Environ Sci Technol*. 2024;58(20):8919–8931. doi:10.1021/acs.est.3c10408
7. Ruan X, Ao J, Ma M, et al. Nanoplastics detected in commercial sea salt. *Environ Sci Technol*. 2024;58(21):9091–9101. doi:10.1021/acs.est.3c11021
8. Qian N, Gao X, Lang X, et al. Rapid single-particle chemical imaging of nanoplastics by SRS microscopy. *Proc Natl Acad Sci*. 2024;121(3):e2300582121. doi:10.1073/pnas.2300582121
9. Niu S, Liu R, Zhao Q, et al. Quantifying the chemical composition and real-time mass loading of nanoplastic particles in the atmosphere using aerosol mass spectrometry. *Environ Sci Technol*. doi:10.1021/acs.est.3c10286
10. Lin S, Zhang H, Wang C, et al. Metabolomics reveal nanoplastic-induced mitochondrial damage in human liver and lung cells. *Environ Sci Technol*. 2022;56(17):12483–12493. doi:10.1021/acs.est.2c03980
11. Chen X, Xuan Y, Chen Y, et al. Polystyrene nanoplastics induce intestinal and hepatic inflammation through activation of NF-κB/NLRP3 pathways and related gut-liver axis in mice. *Sci Total Environ*. 2024;935:173458. doi:10.1016/j.scitotenv.2024.173458
12. Sun R, Liu M, Xiong F, et al. Polystyrene micro- and nanoplastics induce gastric toxicity through ROS mediated oxidative stress and P62/Keap1/Nrf2 pathway. *Sci Total Environ*. 2024;912:169228. doi:10.1016/j.scitotenv.2023.169228
13. Xu JL, Lin X, Wang JJ, Gowen AA. A review of potential human health impacts of micro- and nanoplastics exposure. *Sci Total Environ*. 2022;851:158111. doi:10.1016/j.scitotenv.2022.158111
14. Sangkham S, Faikhaw O, Munkong N, et al. A review on microplastics and nanoplastics in the environment: their occurrence, exposure routes, toxic studies, and potential effects on human health. *Mar Pollut Bull*. 2022;181:113832. doi:10.1016/j.marpolbul.2022.113832
15. Das A. The emerging role of microplastics in systemic toxicity: involvement of reactive oxygen species (ROS). *Sci Total Environ*. 2023;895:165076. doi:10.1016/j.scitotenv.2023.165076
16. Lee SE, Yi Y, Moon S, Yoon H, Park YS. Impact of micro- and nanoplastics on mitochondria. *Metabolites*. 2022;12(10):897. doi:10.3390/metabo12100897
17. Xu D, Ma Y, Han X, Chen Y. Systematic toxicity evaluation of polystyrene nanoplastics on mice and molecular mechanism investigation about their internalization into Caco-2 cells. *J Hazard Mater*. 2021;417:126092. doi:10.1016/j.jhazmat.2021.126092
18. Lu YY, Lu L, Ren HY, et al. The size-dependence and reversibility of polystyrene nanoplastics-induced lipid accumulation in mice: possible roles of lysosomes. *Environ Int*. 2024;185:108532. doi:10.1016/j.envint.2024.108532
19. Ivleva NP. Chemical analysis of microplastics and nanoplastics: challenges, advanced methods, and perspectives. *Chem Rev*. 2021;121(19):11886–11936. doi:10.1021/acs.chemrev.1c00178
20. Sun X, Xiang T, Xie L, et al. Recent advances in fluorescent nanomaterials designed for biomarker detection and imaging. *Materials Today Bio*. 2025;32:101763. doi:10.1016/j.mtbio.2025.101763
21. Yu Q, Wang Y, Mei R, Yin Y, You J, Chen L. Polystyrene encapsulated SERS tags as promising standard tools: simple and universal in synthesis; highly sensitive and ultrastable for bioimaging. *Anal Chem*. 2019;91(8):5270–5277. doi:10.1021/acs.analchem.9b00038
22. Zhang X, Wang Y, Tong X, et al. Synergistic toxicity of nanoplastics and *Helicobacter pylori* on digestive system in mice. *Ecotoxicol Environ Saf*. 2025;290:117757. doi:10.1016/j.ecoenv.2025.117757
23. Yang YF, Chen CY, Lu TH, Liao CM. Toxicity-based toxicokinetic/toxicodynamic assessment for bioaccumulation of polystyrene microplastics in mice. *J Hazard Mater*. 2019;366:703–713. doi:10.1016/j.jhazmat.2018.12.048
24. Gray EP, Coleman JG, Bednar AJ, Kennedy AJ, Ranville JF, Higgins CP. Extraction and analysis of silver and gold nanoparticles from biological tissues using single particle inductively coupled plasma mass spectrometry. *Environ Sci Technol*. 2013;47(24):14315–14323. doi:10.1021/es403558c

25. Laycock A, Clark NJ, Clough R, Smith R, Handy RD. Determination of metallic nanoparticles in biological samples by single particle ICP-MS: a systematic review from sample collection to analysis. *Environ Sci: Nano*. 2022;9(2):420–453. doi:10.1039/D1EN00680K
26. Fernández-Trujillo S, Jiménez-Moreno M, Rodríguez-Fariñas N, Rodríguez Martín-Doimeadios RC. Critical evaluation of the potential of ICP-MS-based systems in toxicological studies of metallic nanoparticles. *Anal Bioanal Chem*. 2024;416(11):2657–2676. doi:10.1007/s00216-024-05181-4
27. Tinggi U, Reilly C, Hahn S, Capra MJ. Comparison of wet digestion procedures for the determination of cadmium and lead in marine biological tissues by zeeman graphite furnace atomic absorption spectrophotometry. *Science of the Total Environment*. 1992;125:15–23. doi:10.1016/0048-9697(92)90378-6
28. Yang L, Yao C, Su Z, et al. Combination of disulfiram and copper−cysteamine nanoparticles induces mitochondria damage and promotes apoptosis in endometrial cancer. *Bioactive Materials*. 2024;36:96–111. doi:10.1016/j.bioactmat.2024.02.009
29. Wang K, Du Y, Li P, et al. Nanoplastics causes heart aging/myocardial cell senescence through the Ca2+/mtDNA/cGAS-STING signaling cascade. *J Nanobiotechnol*. 2024;22(1):96. doi:10.1186/s12951-024-02375-x
30. Liang B, Deng Y, Zhong Y, et al. Gastrointestinal incomplete degradation exacerbates neurotoxic effects of PLA microplastics via oligomer nanoplastics formation. *Adv Sci (Weinh Baden-Wurtt Ger)*. 2024;11(28):e2401009. doi:10.1002/advs.202401009
31. Wu Q, Liu C, Liu D, et al. Polystyrene nanoplastics-induced lung apoptosis and ferroptosis via ROS-dependent endoplasmic reticulum stress. *Science of the Total Environment*. 2024;912:169260. doi:10.1016/j.scitotenv.2023.169260
32. Banerjee A, Shelver WL. Micro- and nanoplastic induced cellular toxicity in mammals: a review. *Science of the Total Environment*. 2021;755:142518. doi:10.1016/j.scitotenv.2020.142518
33. Nguyen B, Tufenkji N. Single-particle resolution fluorescence microscopy of nanoplastics. *Environ Sci Technol*. 2022;56(10):6426–6435. doi:10.1021/acs.est.1c08480
34. Huang Y, Liang B, Li Z, et al. Polystyrene nanoplastic exposure induces excessive mitophagy by activating AMPK/ULK1 pathway in differentiated SH-SY5Y cells and dopaminergic neurons in vivo. *Part Fibre Toxicol*. 2023;20(1):44. doi:10.1186/s12989-023-00556-4
35. Xu D, Ma Y, Peng C, et al. Differently surface-labeled polystyrene nanoplastics at an environmentally relevant concentration induced Crohn's ileitis-like features via triggering intestinal epithelial cell necroptosis. *Environ Int*. 2023;176:107968. doi:10.1016/j.envint.2023.107968
36. Wan S, Wang X, Chen W, et al. Exposure to high dose of polystyrene nanoplastics causes trophoblast cell apoptosis and induces miscarriage. *Part Fibre Toxicol*. 2024;21(1):13. doi:10.1186/s12989-024-00574-w
37. Zhang Z, Xu M, Wang L, et al. Continuous oral exposure to micro- and nanoplastics induced gut microbiota dysbiosis, intestinal barrier and immune dysfunction in adult mice. *Environ Int*. 2023;182:108353. doi:10.1016/j.envint.2023.108353
38. Zhou C, Wu H, Zhang L, et al. Intestinal barrier damage and growth retardation caused by exposure to polystyrene nanoplastics through lactation milk in developing mice. *Nanomaterials*. 2025;15(1):69. doi:10.3390/nano15010069
39. Hsu WH, Chen YZ, Chiang YT, et al. Polystyrene nanoplastics disrupt the intestinal microenvironment by altering bacteria-host interactions through extracellular vesicle-delivered microRNAs. *Nat Commun*. 2025;16(1):5026. doi:10.1038/s41467-025-59884-y
40. Jiang B, Zhao Y, Cao Y, Sun C, Lu W, Fang Y. Advances in the interaction between food-derived nanoparticles and the intestinal barrier. *J Agric Food Chem*. 2024;72(7):3291–3301. doi:10.1021/acs.jafc.3c08145
41. Shiu HT, Pan X, Liu Q, et al. Dietary exposure to polystyrene nanoplastics impairs fasting-induced lipolysis in adipose tissue from high-fat diet fed mice. *Journal of Hazardous Materials*. 2022;440:129698. doi:10.1016/j.jhazmat.2022.129698
42. Wang Y, Xu K, Gao X, et al. Polystyrene nanoplastics with different functional groups and charges have different impacts on type 2 diabetes. *Part Fibre Toxicol*. 2024;21(1):21. doi:10.1186/s12989-024-00582-w
43. Tong X, Li B, Li J, et al. Polyethylene microplastics cooperate with *Helicobacter pylori* to promote gastric injury and inflammation in mice. *Chemosphere*. 2022;288:132579. doi:10.1016/j.chemosphere.2021.132579
44. Chen J, Chen X, Xuan Y, et al. Surface functionalization-dependent inflammatory potential of polystyrene nanoplastics through the activation of MAPK/NF-κB signaling pathways in macrophage raw 264.7. *Ecotoxicol Environ Saf*. 2023;251:114520. doi:10.1016/j.ecoenv.2023.114520
45. Fan Z, Zhang Y, Fang Y, et al. Polystyrene nanoplastics induce lipophagy via the AMPK/ULK1 pathway and block lipophagic flux leading to lipid accumulation in hepatocytes. *J Hazard Mater*. 2024;476:134878. doi:10.1016/j.jhazmat.2024.134878
46. Yu Z, Fan X, Zhao X, et al. Polystyrene nanoplastics induce lipid metabolism disorder by activating the PERK-ATF4 signaling pathway in mice. *ACS Appl Mater Interfaces*. 2024;16(27):34524–34537. doi:10.1021/acsami.4c04416
47. Chen J, Xu Z, Liu Y, Mei A, Wang X, Shi Q. Cellular absorption of polystyrene nanoplastics with different surface functionalization and the toxicity to RAW264.7 macrophage cells. *Ecotoxicol Environ Saf*. 2023;252:114574. doi:10.1016/j.ecoenv.2023.114574
48. Yan L, Yu Z, Lin P, et al. Polystyrene nanoplastics promote the apoptosis in Caco-2 cells induced by okadaic acid more than microplastics. *Ecotoxicol Environ Saf*. 2023;249:114375. doi:10.1016/j.ecoenv.2022.114375
49. Ding R, Chen Y, Shi X, et al. Size-dependent toxicity of polystyrene microplastics on the gastrointestinal tract: oxidative stress related-DNA damage and potential carcinogenicity. *Sci Total Environ*. 2024;912:169514. doi:10.1016/j.scitotenv.2023.169514
50. Li L, Lv X, He J, et al. Chronic exposure to polystyrene nanoplastics induces intestinal mechanical and immune barrier dysfunction in mice. *Ecotoxicol Environ Saf*. 2024;269:115749. doi:10.1016/j.ecoenv.2023.115749
51. Liu W, Zeng M, Zhan C, Wen J, Wang J. Polystyrene nanoplastics exert cardiotoxicity through the notch and wnt pathways in zebrafish (*Danio rerio*). *Sci Total Environ*. 2024;934:173253. doi:10.1016/j.scitotenv.2024.173253
52. Shi B, Xu T, Chen T, Xu S, Yao Y. Co-exposure of decabromodiphenyl ethane and polystyrene nanoplastics damages grass carp (*Ctenopharyngodon idella*) hepatocytes: focus on the role of oxidative stress, ferroptosis, and inflammatory reaction. *Sci Total Environ*. 2024;940:173575. doi:10.1016/j.scitotenv.2024.173575
53. Yang T, Nowack B. A meta-analysis of ecotoxicological hazard data for nanoplastics in marine and freshwater systems. *Environ Toxicol Chem*. 2020;39(12):2588–2598. doi:10.1002/etc.4887
54. Bergami E, Pugnalini S, Vannuccini ML, et al. Long-term toxicity of surface-charged polystyrene nanoplastics to marine planktonic species *Dunaliella tertiolecta* and *Artemia franciscana*. *Aquatic Toxicology*. 2017;189:159–169. doi:10.1016/j.aquatox.2017.06.008
55. Stábile F, Ekvall T, et al. Fate and biological uptake of polystyrene nanoparticles in freshwater wetland ecosystems. *Environ Sci: Nano*. 2024;11(8):3475–3486. doi:10.1039/D3EN00628J
56. Ekvall MT, Stábile F, Hansson LA. Nanoplastics rewire freshwater food webs. *Commun Earth Environ*. 2024;5(1):1–7. doi:10.1038/s43247-024-01646-7

57. Mason SA, Welch VG, Neratko J. Synthetic polymer contamination in bottled water. *Front Chem*. 2018;6:407. doi:10.3389/fchem.2018.00407
58. Liu S, He Y, Yin J, Zhu Q, Liao C, Jiang G. Neurotoxicities induced by micro/nanoplastics: a review focusing on the risks of neurological diseases. *J Hazard Mater*. 2024;469:134054. doi:10.1016/j.jhazmat.2024.134054